RESEARCH ARTICLE

3D bioprinting of in vitro porous hepatoma models: establishment, evaluation, and anticancer drug testing

Xiaoyuan Wang[1] · Zixian Liu[1,2] · Qianqian Duan[1,2] · Boye Zhang[1,2] · Yanyan Cao[1,3] · Zhizhong Shen[1,3] · Meng Li[1,4] · Yanfeng Xi[5] · Jianming Wang[6] · Shengbo Sang[1,2]

Abstract

Traditional tumor models do not tend to accurately simulate tumor growth in vitro or enable personalized treatment and are particularly unable to discover more beneficial targeted drugs. To address this, this study describes the use of three-dimensional (3D) bioprinting technology to construct a 3D model with human hepatocarcinoma SMMC-7721 cells (3DP-7721) by combining gelatin methacrylate (GelMA) and poly(ethylene oxide) (PEO) as two immiscible aqueous phases to form a bioink and innovatively applying fluorescent carbon quantum dots for long-term tracking of cells. The GelMA (10%, mass fraction) and PEO (1.6%, mass fraction) hydrogel with 3:1 volume ratio offered distinct pore-forming characteristics, satisfactory mechanical properties, and biocompatibility for the creation of the 3DP-7721 model. Immunofluorescence analysis and quantitative real-time fluorescence polymerase chain reaction (PCR) were used to evaluate the biological properties of the model. Compared with the two-dimensional culture cell model (2D-7721) and the 3D mixed culture cell model (3DM-7721), 3DP-7721 significantly improved the proliferation of cells and expression of tumor-related proteins and genes. Moreover, we evaluated the differences between the three culture models and the effectiveness of antitumor drugs in the three models and discovered that the efficacy of antitumor drugs varied because of significant differences in resistance proteins and genes between the three models. In addition, the comparison of tumor formation in the three models found that the cells cultured by the 3DP-7721 model had strong tumorigenicity in nude mice. Immunohistochemical evaluation of the levels of biochemical indicators related to the formation of solid tumors showed that the 3DP-7721 model group exhibited pathological characteristics of malignant tumors, the generated solid tumors were similar to actual tumors, and the deterioration was higher. This research therefore acts as a foundation for the application of 3DP-7721 models in drug development research.

Keywords 3D bioprinting · Hepatoma tumor models · Drug screening · Antitumor drug development

Introduction

Hepatoma is one of the most prevalent malignant tumors globally and can metastasize to the lung, brain, bone, and other secondary tissues, which is the primary cause of death from this cancer [1–3]. The increasing incidence and mortality of liver cancer have led to the establishment of effective tumor bionic systems that can carefully explore the pathology and treatment of tumors.

In vitro tumor models are powerful tools for basic biological studies exploring the interaction between tumors and the microenvironment and can also serve as platforms for

✉ Shengbo Sang
  sunboa-sang@tyut.edu.cn

1 Shanxi Key Laboratory of Micro Nano Sensors and Artificial Intelligence Perception, College of Electronic Information and Optical Engineering, Taiyuan University of Technology, Taiyuan 030024, China

2 Key Lab of Advanced Transducers and Intelligent Control System of the Ministry of Education, Taiyuan University of Technology, Taiyuan 030024, China

3 Shanxi Institute of 6D Artificial Intelligence Biomedical Science, Taiyuan 030031, China

4 Shanxi-Zheda Institute of Advanced Materials and Chemical Engineering, Taiyuan 030024, China

5 Department of Pathology, Shanxi Provincial Cancer Hospital, Taiyuan 030024, China

6 General Hospital of Taiyuan Iron and Steel Company, Taiyuan 030809, China

screening anticancer drugs [4, 5]. Currently, animal models and in vitro two-dimensional (2D) models are the main types of classical tumor models. However, 2D models are limited by being unable to simulate the internal structure and microenvironment of cells [6–8], and animal models have problems such as ethical disputes, cumbersome operation, high cost, and poor reproducibility [9, 10]. Therefore, these current models cannot usually establish large-scale and complex structures, and it is consequently difficult to accurately simulate the growth of organs and tumors in vitro [11, 12]. However, three-dimensional (3D) tumor models can compensate for some of the insufficiencies of 2D and animal models [13–15]. 3D bioprinting can form into grid-like 3D structures for loading with cells and is more economically efficient and biocompatible with a higher percentage of cell survival than the conventional 2D culture methods. 3D models can be constructed with extremely fine structures and complex biological components, and 3D bioprinting has therefore been widely used for modeling various tissues/organs and diseases during the past 10 years [16, 17].

Recently, the multifunctional technology of establishing accurate models to reproduce the complexity of the tumor microenvironment has been applied to the study of cancer occurrence, development, metastasis, and drug response [18–20]. Although 3D bioprinting technology has made significant progress, several challenges remain. For example, although the dense grid of biomaterials encapsulating tumor cells can maintain the mechanical strength of the ink and the structural fidelity of the bioprinted model, this can also limit the diffusion, migration, and proliferation of the tumor cells [21, 22]. Therefore, the generation of functional tumor tissue could be promoted if the bioprinting-based hydrogel scaffolds contain interconnected holes that enable effective diffusion of oxygen, nutrients, and waste and movement of cells [23–25]. Recently, two incompatible bioinks were described [26, 27] that can construct porous cell-loaded hydrogels at the micro- and nanoscale, and the resulting hydrogel can be 3D printed to a specific geometry. Although the micropores of this hydrogel network are conducive to cell proliferation, migration, and growth, the utility of such a pore-forming bioink toward liver tumor models has not been previously demonstrated.

The current cell imaging and detection methods for cell proliferation, migration, and drug screening in in vitro tumor models include protocols such as 4′,6-diamidino-2-phenylindole (DAPI), live/dead, and phalloidin staining [28, 29]. However, these dyes are disadvantaged by their high cost and lack of reusability. Fluorescent carbon quantum dots (CDs) have the advantages of low cost, raw material abundance, high reproducibility, and favorable optical performance, biocompatibility, and stability to enable long-term tracking and observation [30–33]. CDs can be considered for use in the assessment of cell proliferation in 3D printing, cell migration, and drug screening.

In this study, we established a 3D porous liver cancer (SMMC-7721) model (3DP-7721) composed of a new type of bioink that comprised 3D bioprinting of SMMC-7721 cells with an aqueous two-phase emulsion of two biocompatible solutions gelatin methacrylate (GelMA) and poly(ethylene oxide) (PEO) (Fig. 1a). The pore size, Young's modulus, swelling ratio, and porosity of GelMA-PEO hydrogels with different volume ratios were investigated. The 3DP-7721 model was compared with the 2D culture (2D-7721) and the 3D mixed culture model (3DM-7721) (Fig. 1b). In the three models, SMMC-7721 cells were stained with CDs for cell tracking. The biological characteristics of the three models were evaluated by detecting cell proliferation, tumor markers, and related protein and gene expression. The differences between the three culture models and the effect of antitumor medication on each model were assessed. The tumorigenic performance of each model was also investigated. The 3DP-7721 model developed in this work could potentially serve as a foundation for its use in drug development research.

Experiments

Materials and characterization

L-cysteine, penicillin-streptomycin, m-phenylenediamine, gelatin from porcine skin, rhodamine B, lithium phenyl-(2,4,6-trimethylbenzoyl) phosphine (LAP, photoinitiator), and dimethyl sulfoxide were obtained from Sinopharm Ltd. (China). Gibco (Singapore) supplied the fetal bovine serum, phosphate-buffered saline (PBS), and trypsin–EDTA. Minimum essential medium (MEM) was purchased from Cytiva (China). PEO (average M_v about 300,000 (nominal), powder), paraformaldehyde, goat serum blocking fluid, and methacrylic anhydride were purchased from Macklin (Shanghai, China). Shanghai Canspec Scientific Instruments Co., Ltd. (China) provided dialysis bag MD34 (molecular weight cutoff: 8–14 kDa) and doxorubicin hydrochloride (DOX). Abclonal Technology (Wuhan, China) supplied the albumin (ALB), alpha-fetal protein (AFP), proliferation marker protein Ki-67 (Ki67), and a member of the cytochrome p450 oxidase family (CYP3A4) immunofluorescence kits. DAPI and the cell counting kit-8 (CCK-8) were obtained from BestBio (Shanghai, China), and SMMC-7721 cells were obtained from Wuhan Procell Life Technology Co., Ltd. (China). All reagents were of analytical grade and could be used immediately. The UPT-II apparatus (Shanghai Yiheng Scientific Instrument Company, Shanghai, China) was used to obtain the deionized ultra-pure water.

A uniaxial compression apparatus was used to determine the Young's modulus of the scaffolds (Norwood
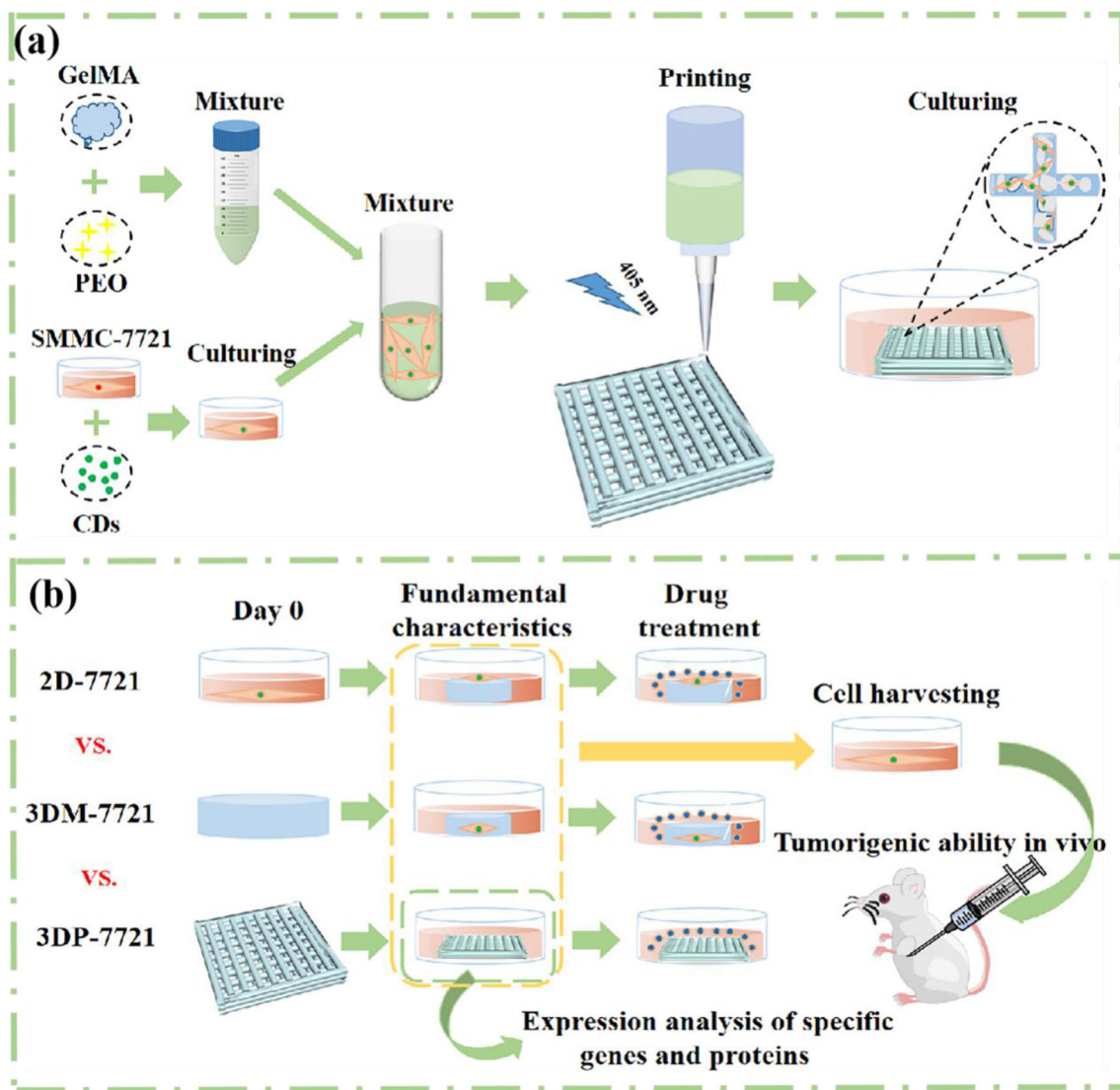
Fig. 1 Experimental process and detection flow chart. **a** Schematic of the bioink composition, 3D printing process, and structural crosslinking. **b** Comparison between the establishment of 2D-7721, 3DM-7721, and 3DP-7721 models to evaluate drug resistance. SMMC-7721: human hepatocarcinoma cells; 3D: three-dimensional; 2D-7721: two-dimensional culture model; 3DM-7721: 3D mixed culture model; 3DP-7721: 3D bioprinting model; GelMA: gelatin methacrylate; PEO: poly(ethylene oxide); CDs: carbon quantum dots

5556 Research Institute, USA). A Cytation5 imaging reader (BioTek, USA) was used to image cell morphology. The 3D-Bioplotter (Envision TEC GmbH, Germany) was used for printing. The purity and quantity of RNA were established using a NanoDrop One^c spectrophotometer (Thermo Scientific, USA). PrimeScript™ RT Master Mix (Takara, Japan) was used to synthesize cDNA from RNA. Real-time quantitative polymerase chain reaction (RT-qPCR) analysis was performed using the Premix Ex Taq™ II (Takara, Japan) and Biosystems™ QuantStudio™ 6 Flex RT-PCR System.

Preparation of carbon quantum dots and bioink

CDs M-phenylenediamine (0.3 g) and l-cysteine (0.675 g) were dissolved in 30 mL of double distilled water. The mixture was placed into a 50-mL autoclave with Teflon lining and placed in a box-type resistance furnace for 10 h at 160 °C. After the system was cooled to room temperature, the CDs solution was obtained by filtration through a 0.22 μm membrane. The filtrate was further purified by deionized hydrodialysis (molecular weight cutoff (MWCO) 3.5 kDa). The resulting mixture was dried under vacuum. Finally, the pure CDs were gathered and stored at 4 °C.

GelMA The preparation of GelMA was based on previous studies [34, 35]. Briefly, 200 mL of PBS was added and

heated to 50 °C in a water bath, and then 10 g of gelatin was added and stirred until this was completely dissolved. Then, 16 mL of methacrylic anhydride was slowly added at an average rate of 1 mL/min. Add 800 mL PBS to the above solution and heat it in a 50 °C water bath for 2 h, and then agitate for 10 min. After that, the above solution was placed in a dialysis bag (MWCO 8–14 kDa) for dialysis for 5 d, followed by a 10-min centrifugation at 4000 r/min of the dialyzed solution. The supernatant after centrifugation was lyophilized to obtain pure GelMA, which was stored at −20 °C.

Bioink LAP powder was added to PBS solution preheated at 50 °C to obtain the LAP solution (0.5%, mass fraction). Then, 1 g GelMA was added to 10 mL of LAP solution to obtain 10% (mass fraction) GelMA solution, and 0.16 g PEO was added to 10 mL of LAP solution to obtain 1.6% (mass fraction) PEO solution. The above-obtained GelMA solution and PEO solution were mixed in different proportions. The mixed solutions were heated in a 50 °C water bath and stirred evenly for subsequent use.

Performance characterization of different proportions of bioinks

Preparation of gradient gel columnar scaffolds

Solutions of GelMA (10%, mass fraction)/PEO (1.6%, mass fraction) at 1:1, 2:1, 3:1, and 4:1 volume ratios and that of standard GelMA (10%) were prepared. The solutions were illuminated with ultraviolet (UV) blue light (about 405 nm, 20 W/cm^2) for 15 s for curing and crosslinking to create a 5 mm-high and 8 mm-wide cylinder.

Young's modulus test

A uniaxial compression test was used to assess the mechanical strength of GelMA-PEO hydrogels with various ratios. To evaluate the compressive performance, cylindrical scaffolds (8 mm diameter and 5 mm height) were built and then tested on a mechanical test platform (Instron 3343, Instron Instruments, USA) equipped with a 1 kN load cell. The compression rate used during testing for all scaffolds was 0.5 mm/min. The slope of the initial linear areas (0%–4%) of the compressive stress–strain curve was used to calculate the compressive modulus.

Swelling property

Different ratios of GelMA-PEO gel columnar scaffolds were prepared (n=5 for each ratio). Each sample was supplemented with 4 mL of PBS (pH 7.4) and was then placed at 37 °C. After different time periods (6, 12, 18, 24, 30, 36, 42, and 48 h), the PBS was removed (using filter paper to remove any leftover water droplets), and the sample mass (W_1) was

weighed in a Petri dish. Each sample was freeze-dried, and the lyophilized samples were weighed again (W_2) with a Petri dish. The swelling ratio was obtained with the following formula:

$$Q_s = (W_1 - W_2)/W_2 \times 100\%.$$

Porosity

Weight (W_3) and volume (V) of the dried hydrogel scaffold were measured, and each sample was placed in 2 mL of alcohol, soaked for 4 h, and then kept at 37 °C to achieve swelling equilibrium. The excess solution was removed with a filter paper, and the sample was weighed (W_4) in a Petri dish. The porosity was calculated as follows:

$$\frac{(W_4 - W_3/\rho)}{V} \times 100\%,$$

where ρ is the density of the aqueous solution.

Construction of the 3DP-7721 model

To obtain the GelMA-PEO (3:1 volume ratio) mixed solution, a total of 50 μL CDs (20 mg/mL) were added to SMMC-7721 cells and incubated for 30 min (37 °C). CD-stained cells were mixed with GelMA-PEO to produce a final cell suspension of 5×10^5 cells/mL. To defoam the mixture of cells and biological material, 3 mL was injected into a sterile syringe fitted with a 30 G needle (160 μm). The syringe was deaerated and then placed in a 3D printer for 30 min at a 20 °C barrel temperature. The printing parameters were a barrel temperature of 20 °C, platform temperature of 0 °C, needle offset of 0.128 mm, pressure of 1.3 bar (1 bar=100 kPa), post-flow of 0 s, speed of 13.0 mm/s, pre-flow of 0 s, waiting time between layers of 15 s (optical crosslinking time of each layer after printing, about 405 nm, 20 W/cm^2), minimum length of 0.4 mm, density of 1.00 g/cm^3), and a Petri dish of 35 mm diameter to collect the printed structure. The printed model was then filled with 2 mL of the previously generated medium and was incubated at 37 °C and 5% CO$_2$. The medium was changed every two days.

Collagenase was added to the medium for degradation (2 mg/mL, 0.5 h) and filtered through a 70 μm filter to avoid the formation of clumps or particles from undigested polymers. The suspension was centrifuged at 2000 r/min for 5 min, and the supernatant was discarded. Digested cells were counted with a cell counting board to confirm that the number of cells in the subsequent printed model was 1×10^5.

Construction of 3DM-7721 model

GelMA-PEO (3:1 volume ratio) was prepared, and 50 µL CDs (20 mg/mL) were added to SMMC-7721 cells and incubated for 30 min. CDs-stained cells were mixed with GelMA-PEO to make a cell suspension for defoaming treatment at a final cell density of 5×10^5 cells/mL. Cell suspension (200 µL) was added per well in a 24-well plate and photocured and crosslinked to prepare a 3DM-7721 model. The number of cells compared in each of the three models was 1×10^5.

Cell proliferation assay

The cell morphology of the 2D-7721, 3DM-7721, and 3DP-7721 models was detected using a Cytation5 imaging reader on Days 1, 4, 8, and 12. Cells were then incubated in a mixture of 10:1 volume ratio of medium and CCK-8 reagent. Also, 100 µL of combined solution was transferred into a new 96-well plate and incubated for 2 h at 37 °C before the absorption was measured at 450 nm. Cells cultivated in the 2D-7721, 3DM-7721, and 3DP-7721 models were compared for growth and viability.

Protein and mRNA expression

The 3DP-7721 model was cultured for 7 d, washed with PBS three times, and then immunofluorescence staining was performed for AFP, Ki67, CYP3A4, and ALB. The Cytation5 imaging reader was used to obtain fluorescence images.

For analysis of gene expression, collagenase II was added to 3DP-7721 medium for degradation (2 mg/mL, 0.5 h) and was 70 µm filtered to remove undigested polymer clots or particles. The suspension was centrifuged at 1200 r/min for 5 min, and the supernatant was discarded to collect the isolated cells. Disrupted samples were then treated with frozen Trizol reagent and allowed to stand for 15 min with intermittent shaking in between to isolate total RNA. cDNA was synthesized from extracted RNA with the PrimeScript™ RT Master Mix kit. RT-qPCR was performed with TB Green Premix Ex Taq™ II (Takara, Japan) on an applied Biosystems™ QuantStudio™ 6 Flex RT-PCR System and was used to identify the mRNA expression of tumor-related proteins, genes, and drug-resistant genes, including alpha-fetal protein (AFP), transforming growth factor beta (TGF-β), prominin-1 (*CD133*), epithelial cell adhesion molecule (*EpCAM*), interleukin-8 (*IL-8*), cluster of differentiation 24 (*CD24*), multidrug resistance-associated protein 1 (MRP1), multidrug resistance-associated protein 2 (MRP2), breast cancer resistant protein (BCRP), atp binding cassette subfamily b member 1 gene (*ABCB1*), multidrug resistance 1 (*MDR-1*), and epidermal growth factor receptor (*EGFR*). Using the $2^{-\Delta\Delta C_T}$ technique, the relative gene expression levels of these genes were computed [36]. Primer sequences and antibody information are presented in Tables S1 and S2 (Supplementary Information). Gene expression was standardized to that of recombinant human beta-actin (β-Actin) with 40 cycles for all RT-qPCR analyses. Data are shown as mean± standard deviation (*n*=3).

Pharmacodynamic evaluation of antitumor drugs

After 12 d of culture, the 3DP-7721 model contained 6×10^6 cells, and the same number of CD-stained SMMC-7721 cells was seeded into a 24-well plate and columnar scaffold. The three cell models were incubated with DOX (0, 2.5, 5, 10, 20, and 40 µg/mL), luteolin (0, 40, 80, 120, 160, and 200 µg/mL), or cisplatin (0, 1.5, 10, 20, 40, and 80 mg/mL) for 48 h. The Cytation5 imaging reader was used to image the fluorescence. Cell growth was measured using the CCK-8 assay.

Tumorigenic ability

In vivo tumorigenicity assays were performed using athymic nude mice (male, 5–6 weeks old, 18–25 g). All animal procedures were performed in accordance with the Guidelines for Care and Use of Laboratory Animals of Shanxi Medical University and approved by the Animal Ethics Committee of the First Hospital of Shanxi Medical University (License number: SYXK (Jin) 2018–0001). 2D-7721, 3DM-7721, and 3DP-7721 (each with 1×10^6 SMMC-7721 cells) were prepared as described above and cultured in medium for 7 d. Type II collagenase was added to the medium for degradation (2 mg/mL, 0.5 h), which was then 70 µm filtered to remove any clumps. The suspension was centrifuged for 5 min at 2000 r/min, and the supernatant was removed. ABW® Matrigen gel was mixed with PBS at 1:1 volume ratio (at 4 °C), and then cells were added to form a suspension. The cell suspension (100 µL for each mouse) was injected into the armpit of nude mice (three mice for each model) using a syringe (precooled at 4 °C). Animals were housed in specific pathogen-free (SPF) animal cages with free access to water and food. Tumor volume and mouse weight were calculated during the one-month period after tumor formation (Days 0, 3, 6, 9, 12, 15, 18, and 21). Nude mice were euthanized by cervical dislocation 21 days later, and the tumors were excised, photographed, and weighed. Tumor specimens were embedded in paraffin and sectioned into 5-µm-thick slices for hematoxylin and eosin (HE) staining and immunohistochemical staining with Ki67, *EpCAM*, *CD133*, and terminal deoxynucleotidyl transferase-mediated dUTP-biotin nick end labeling assay (TUNEL) (human only), and then restained with DAPI and observed under fluorescence microscope.

Statistical analysis

All data were statistically analyzed using one-way analysis of variance in SPSS 17.0. Data are expressed as mean± standard deviation. Significance is indicated by $^*p < 0.05$, $^{**}p < 0.01$, and $^{***}p < 0.001$.

Results and discussion

Characterizations of the hydrogel constructs

The porous hydrogel structures composed of GelMA and PEO in different proportions are shown in Fig. 2. Under a fluorescence microscope, the surface of the standard GelMA hydrogel lacked any visible micropores (Fig. 2a). Micropores were interconnected and evenly distributed in the structure of GelMA-PEO hydrogel stained by rhodamine B. The average pore size of the hydrogel decreased with the volume proportion of PEO. Therefore, the pore size could be modified by adjusting the volume fraction of PEO. The average particle size was calculated to be (55.96±0.68), (34.81±0.81), (17.46±0.21), and (7.58±0.15) μm from 100 particles of each hydrogel at a GelMA-PEO ratio of 1:1, 2:1, 3:1, and 4:1, respectively (Figs. 2f–2i). GelMA-PEO porous hydrogel structures in different proportions were lyophilized and characterized using scanning electron microscopy (SEM) (Fig. S1 in Supplementary Information). The particle size of the hydrogel structure under SEM was comparable with that observed under fluorescence microscope, indicating that the micro-/nanopore structure of the hydrogel structure has high stability.

Cell migration, dissemination, proliferation, and differentiation are significantly influenced by the mechanical properties of the microenvironment [37]. The influence of the micro-/nanopore framework on the mechanical attributes of the hydrogel structure composed of various ratios of GelMA to PEO was investigated using a mechanical analyzer in the unconfined compression mode. When the hydrogel structure was unconfinedly compressed at room temperature, the hydrogel structure exhibited a nonlinear stress–strain response (Fig. 3a). The stress–strain curve shows that under the same compressive stress, the mechanical strain of the nanoporous hydrogel structure before fracture was higher than that of the standard hydrogel structure. The Young's modulus of the standard GelMA hydrogel (5%, mass fraction) was 1.69 kPa (Fig. 3b). After adding PEO, the mechanical properties were enhanced. However, as the volume ratios of GelMA (10%, mass fraction) to PEO (1.6%, mass fraction) increased, the Young's modulus increased, and the mechanical properties of the stent were significantly enhanced. The Young's moduli of the porous GelMA hydrogels with multiple compositions were 5% higher than the standard Young's

modulus. The stress–strain curves and Young's modulus (Figs. S2a and S2b in Supplementary Information) were compared after immersion of hydrogels in PBS for 24 h with those before immersion (Figs. 3a and 3b). The Young's modulus decreased to a certain extent (about 50%) after immersing in PBS for 24 h because the PEO underwent leaching during this time and formed pores.

Cells thrive in a nutrient- and water-rich environment, e.g., in a hydrogel, which has the ability to absorb water. As shown in Fig. 3, the swelling ratio and porosity of GelMA and PEO scaffolds with different volume ratios were measured. The gel reached swelling equilibrium 36 h after the addition of PBS. After adding PEO to the standard GelMA, the swelling ratio and porosity were both improved (Figs. 3c and 3d). The hydrogel became more compact as the quantity of GelMA increased, and the capacity of the hydrogel to absorb water consequently declined (Fig. 3d), which was related to the pore size of the hydrogels of GelMA and PEO with different volume ratios [35]. The test results of the qualities of the scaffolds indicate that the 3D-printed scaffolds could be employed effectively in the following cell research.

Considering the influence of the different volume ratios of GelMA to PEO on the pore size, stress–strain curve, Young's modulus, swelling ratio, and porosity, a 3:1 volume ratio of GelMA to PEO was used for subsequent experiments.

Optimization of printing parameters

The rheological characteristics of bioink affect the printability because a hierarchical micro-/nanopore structure of the hydrogel could be formed from the two immiscible aqueous phases used in the bioink. The rheology of the bioink was influenced by temperature in addition to the volume fraction of PEO. Therefore, to preserve the stability of the porous structure, the printing parameters were studied. The GelMA-PEO hydrogel solidified at a low temperature (<10 °C) and was not smooth at high temperature (>25 °C); thus, the hydrogel was not easy to form, and it was impossible to draw high-precision lines. So, we subsequently chose to print at 20 °C. Figure 4 shows that the integrity of the printing structure was also related to the nozzle movement speed and extrusion pressure. A fast-moving printer nozzle combined with low air pressure produced discontinuities in the printing line, whereas a slow-moving printer nozzle combined with high air pressure ensured accumulation of hydrogel. Thus, to shape the printed structure and draw relatively smooth lines, the 3D bioprinting process was performed at 20 °C with a nozzle moving speed of 13 mm/s and an extrusion pressure of 1.3 bar.
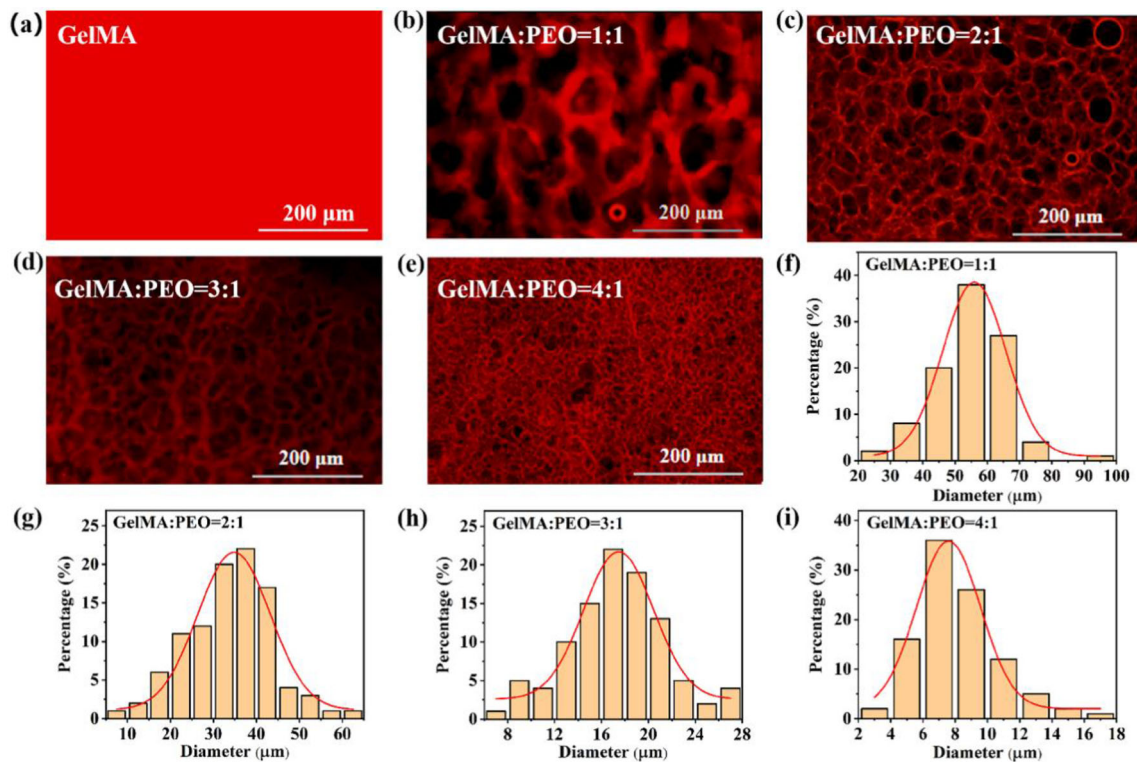
Fig. 2 The volume ratio of GelMA (10%, mass fraction) to PEO (1.6%, mass fraction) has different effects on pore size. **a–e** Fluorescence micrographs and **f–i** particle size distribution histograms of rhodamine B-stained porous hydrogel structure with different volume ratios of GelMA to PEO. GelMA: gelatin methacrylate; PEO: poly(ethylene oxide)

Construction of the 3DP-7721 model

SMMC-7721 cells were incubated with CDs, and then GelMA-PEO hydrogel-carrying cells were used to construct tumor models. CCK-8 tests were used to investigate the activity of SMMC-7721 cells in the models. Figure S3 (Supplementary Information) shows the characterization of the CDs dye used in this study. The CDs fluoresced green under a 365 nm UV lamp (Fig. S3a in Supplementary Information). The viability of cells incubated with different concentrations of CDs for 24 and 48 h was tested. The results show that the cell viability rates reached 86% after being incubated with 100 mg/mL CDs for 48 h, indicating that the CDs have low toxicity and favorable biocompatibility (Fig. S3b in Supplementary Information). The panoramic fluorescence image of the 3D-printed hydrogel-loaded cells incubated with CDs is shown in Fig. S3c (Supplementary Information). Thus, CDs could be used to track cells in 3D printing.

All SMMC-7721 cells stained with CDs exhibited a strong green fluorescence (Fig. 5a). In addition, as the culture time lengthened, the SMMC-7721 cells in the three models exhibited different degrees of proliferation. The SMMC-7721 cells maintained relatively high activity in the three models, which also shows that the GelMA-PEO scaffold had high cell growth potential and strong biocompatibility. The cells were

evenly distributed in the printed lines in the 3DP-7721 model during 1–12 days of culture without breaking the GelMA-PEO hydrogel. The CCK-8 assay was used to compare cell proliferation in 2D-7721, 3DM-7721, and 3DP-7721 models (Fig. 5b). At Day 4, the cell proliferation capacity of the 3DP-7721 model was significantly lower than that of the 2D-7721 model. By Day 8, the number of cells in the 2D-7721 and 3DP-7721 models was equivalent. After eight days, the cell proliferation capacity of the 3DP-7721 model was higher than that of the 2D-7721 model where cells flooded the entire well plate on Day 8, which slowed the cell proliferation. Throughout the culture period, the proliferation of cells in the 3DM-7721 model was lower than that of the other two models, and the 3DP-7721 model was more conducive to cell proliferation and growth. The three culture models showed clearly varied patterns of cell growth, which may have been caused by the varying levels of cell–medium interaction between each model. The cell proliferation may also exhibit hardness-dependent proliferation where cells have higher proliferation ability on hard surfaces [11, 38]. Day 7 after printing was determined to be the most advantageous point for contrasting 3D-printed cells with those grown in planar culture, and we therefore selected this day as the time point for most of the functional assessments, including protein expression and pharmacological investigations.
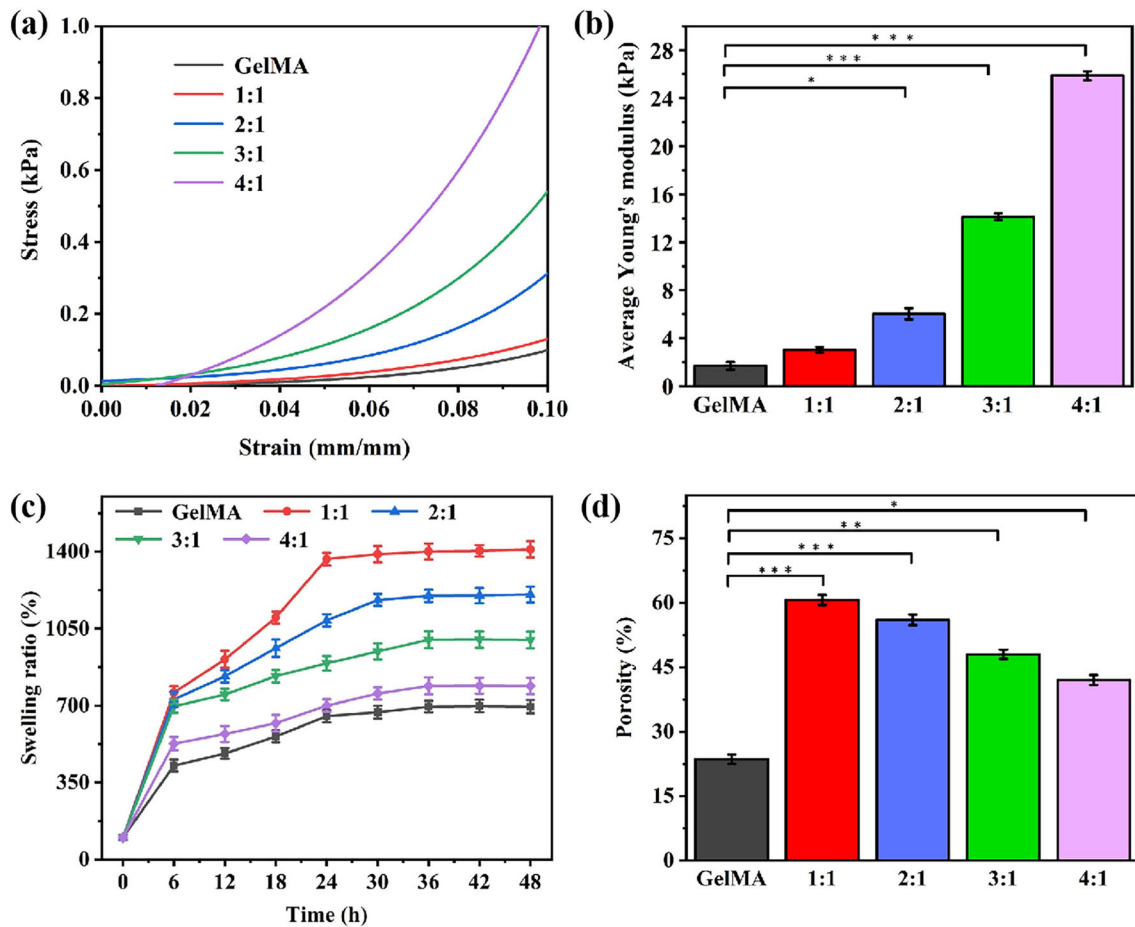
Fig. 3 The **a** stress–strain curves and **b** Young's modulus of the porous hydrogel structure. The **c** swelling ratio and **d** porosity of GelMA and PEO with different volume ratios. Data are presented as mean±standard deviation, $n=3$. $^*p<0.05$, $^{**}p<0.01$, $^{***}p<0.001$. GelMA: gelatin methacrylate; PEO: poly(ethylene oxide)

Liver- and tumor-related protein and mRNA expression

Immunofluorescence was used to identify the expression of several liver-related proteins in the 3DP-7721 model on Day 7. ALB, AFP, Ki67, and CYP3A4 were all shown to be expressed (Fig. 6). Cells were removed from a 2D-7721 model in the logarithmic growth phase, a 3DM-7721 model, or a 3DP-7721 model after 5, 10, and 15 days of culture to examine mRNA expression of proteins and genes relevant to the liver. In comparison with that in the 2D-7721 model, the mRNA expression levels in the 3DP-7721 model of AFP, TGF-β, and *IL-8* were significantly greater and steadily rose during culture. After 15 days of culture, the mRNA expression levels of *EpCAM*, *CD133*, and *CD24* were downregulated (Fig. 7). The expression of these three genes on Day 15 was increased compared with that on Day 1 but decreased from Day 10, whereas the expression of other
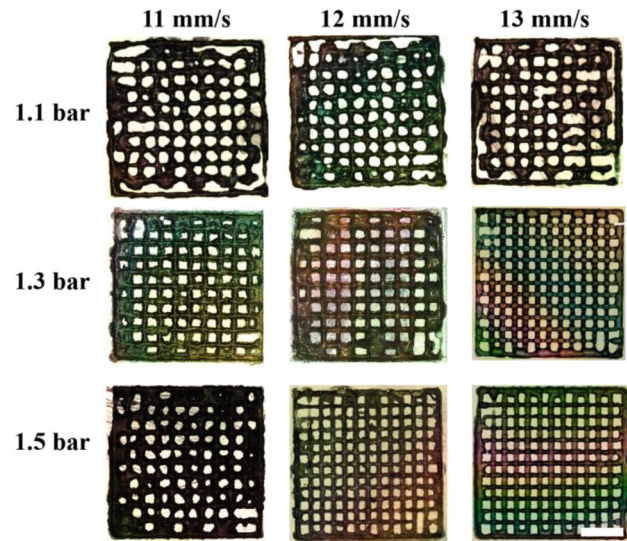

Fig. 4 Optimizing of printing parameters. Panorama of printing under different printing speeds and pressures (1 bar=100 kPa). Scale bar: 3 mm. $n=5$

genes increased; therefore, the cells had not lost their cancerous behavior.

In Fig. 7, the overall expression levels of six types of tumor-related proteins and mRNA expressed in the 3DP-7721 model were higher than those in the 3DM-7721 model. Modifications in cell differentiation and proteins associated with cancer (AFP and TGF-β protein) between cells grown in the three models suggested different biological features (Figs. 7a and 7b). The expression of cancer stem cell markers *CD133* and *EpCAM* was markedly increased in the 3D-printed tumor cells, indicating that these tumor cells exhibited higher drug resistance, invasion, metastasis, and recurrence abilities compared with planar produced cells (Figs. 7c and 7d) [39, 40]. Additionally, we discovered that the 3D-printed tumor model expressed larger amounts of *IL-8* and *CD24*, which meant that its immunosuppressive ability was stronger (Figs. 7e and 7f) [41, 42]. The expression of cancer-related proteins and genes varied among the three models, suggesting that the cells had various biological properties.

Effects of antitumor drugs on the 3DP-7721 model

One of the main goals of our study was to develop an in vitro tumor drug screening system that mimics the in vivo pathophysiology of the tumor microenvironment for tumor studies as well as medication development. DOX, luteolin, and cisplatin are three common antitumor drugs that have killing effects on a variety of tumors [31, 42, 43]. We administered DOX, luteolin, or cisplatin to the 2D-7721, 3DM-7721, and 3DP-7721 models for 48 h to examine how the 3DP-7721 model responded to antitumor medications. In the 3DP-7721 model, the number of SMMC-7721 cells in the model gradually decreased with the increase of the DOX concentration (Fig. 8a and Fig. S4 in Supplementary Information). CCK-8 results showed that the half maximal inhibitory concentration (IC_{50}) values of DOX, luteolin, and cisplatin were the highest in the 3DM-7721 model followed by those in the 3DP-7721 model and were the smallest in the 2D-7721 model (Figs. 8b–8d). The possible reason is that the 2D-7721 model was more likely to be in direct contact with the drug, which consequently had the strongest effect [11, 38]. The 3DP-7721 model was more accessible to the drug than the 3DM-7721 model because of the grid-like structure. The slower cell proliferation and drug penetration in the 3D tumor models made them less sensitive to cytotoxic drugs than 2D cultures, but other more important aspects such as matrix or factors arising from stromal-tumor interactions contribute to drug resistance. Luteolin had the strongest effect on SMMC-7721 cells (Fig. 8c).

We incubated the 2D-7721, 3DM-7721, and 3DP-7721 models with luteolin (120 µg/mL) for 48 h to additionally assess the 3DP-7721 model response to antitumor medications. We investigated the expression of several drug-resistant proteins and genes, including MRP1, *MDR-1*, *ABCB1*, BCRP, MRP2, and *EGFR*. RT-qPCR showed that the expression levels of resistance genes in the three models differed [44]. The expression level of MRP1 protein in the three models of 2D-7721, 3DM-7721 and 3DP-7721 increased significantly with the increase of time (Fig. 9a). The protein and mRNA expression levels of BCRP, *MDR-1*, and MRP2 (Figs. 9b–9d) reached a maximum on Day 10. *ABCB1* and *EGFR* mRNA expression levels (Figs. 9e and 9f) showed an upward trend over time. The overall mRNA expression level in the 3DP-7721 model was higher than that in the 3DM-7721 model. The 3DP-7721 model boosted the expression of *ABCB1*, *MDR-1*, MRP1, and *EGFR*, which may help discover why various drugs had diverse effects in the three cell models. Tumor cells undergo specific changes in gene expression when subjected to pharmacological stress. For instance, the expression of *MDR-1* genes can be upregulated in tumor cells to increase drug efflux [44, 45]. Additionally, by boosting autophagy, tumor cells can eventually tolerate medicines [46, 47]. Therefore, it is hypothesized that following anticancer medication therapy, the expression of drug-resistant genes will increase. Thus, by determining the antitumor effects of drug treatments, variations in the expression levels of different genes were mirrored variations in the biological functions of tumor cells.

In the 3DP-7721 model, SMMC-7721 cells showed higher tumor-related biological activity than the other two culture models. 3DP-7721 models may produce pharmacodynamic results close to what is actually happening in the body, helping to speed up the drug development process and reduce the risk of failure and the cost of drug screening.

In vivo tumorigenicity

To evaluate the tumorigenic potential of the cells in the three models, the same number of SMMC-7721 single cells isolated from the 3DP-7721 model and the 3DM-7721 model, and primary cells cultured in 2D-7721 culture were injected into the subcutaneous tissue of severe combined immunodeficiency mice to generate a cell xenograft tumor model. Without exception, tumors were formed in all three models (Figs. 10a and 10b). The tumor weight varied with model group (Fig. 10c). In addition, the body weight of mice in the 3DP-7721 model group showed an overall upward trend but did not differ in comparison with that of the 2D-7721 culture group (Fig. 10d). The weight and volume of solid tumors generated by the 3DP-7721 group were larger than those generated by the 2D-7721 and 3DM-7721 model groups (Figs. 10c and 10e), which implied that the 3DP-7721 model group had enhanced tumorigenicity.
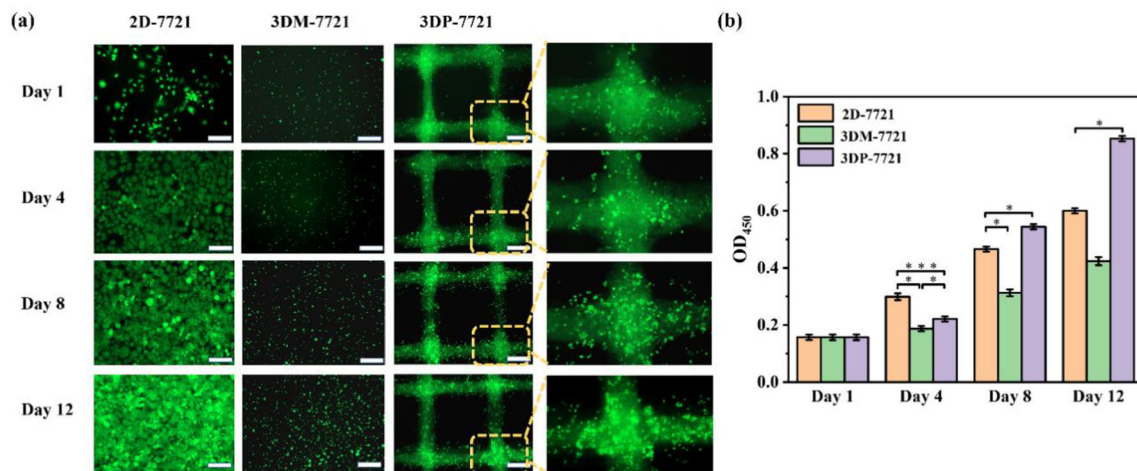
Fig. 5 **a** Fluorescence images of 2D-7721, 3DM-7721, and 3DP-7721 models containing cells incubated with CDs in GelMA-PEO hydrogel on Days 1, 4, 8, and 12. Scale bar: 300 μm. **b** SMMC-7721 cell activity measured via CCK-8 assay. Data are presented as mean±standard deviation, $n=3$. $^{*}p<0.05$, $^{***}p<0.001$. 2D-7721: two-dimensional culture model; 3DM-7721: three-dimensional mixed culture model; 3DP-7721: 3D bioprinting model; CDs: carbon quantum dots; GelMA: gelatin methacrylate; PEO: poly(ethylene oxide); SMMC-7721: human hepatocarcinoma cells; CCK-8: cell counting kit-8; OD$_{450}$: absorbance is measured at 450 nm
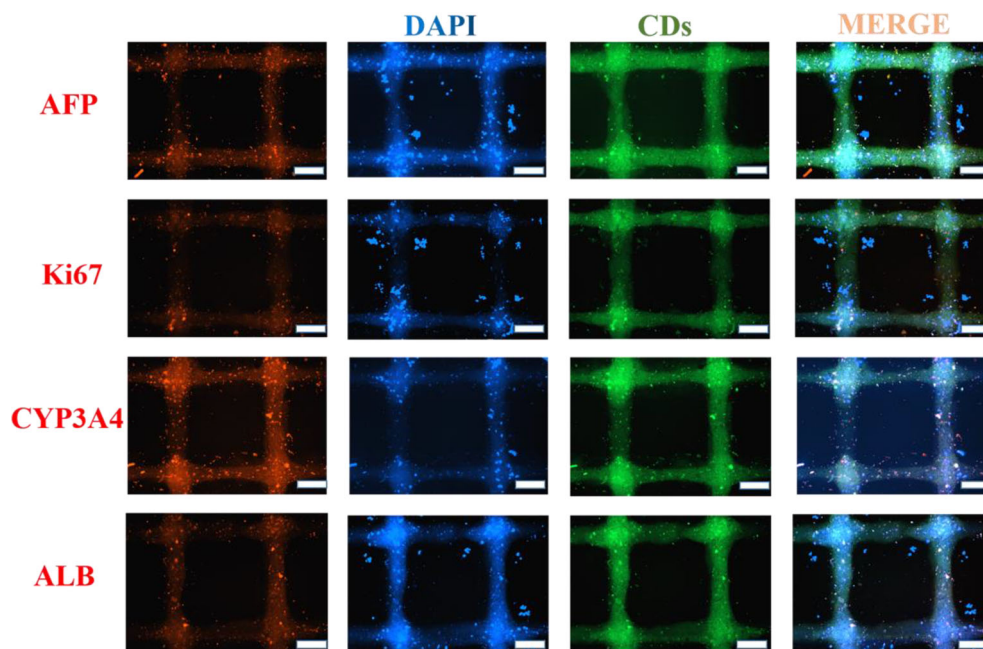
Fig. 6 Expression of liver-related proteins in a model of liver cancer cells made via 3D bioprinting. Expression of AFP, Ki67, CYP3A4, and ALB in the 3DP-7721 model after printing for 7 d is shown. Scale bar: 300 μm. $n=3$. 3D: three-dimensional; ALB: albumin; AFP: alpha-fetal protein; Ki67: proliferation marker protein Ki-67; CYP3A4: a member of the cytochrome p450 oxidase family; 3DP-7721: 3D bioprinting model; DAPI: 4′,6-diamidino-2-phenylindole; CDs: carbon quantum dots
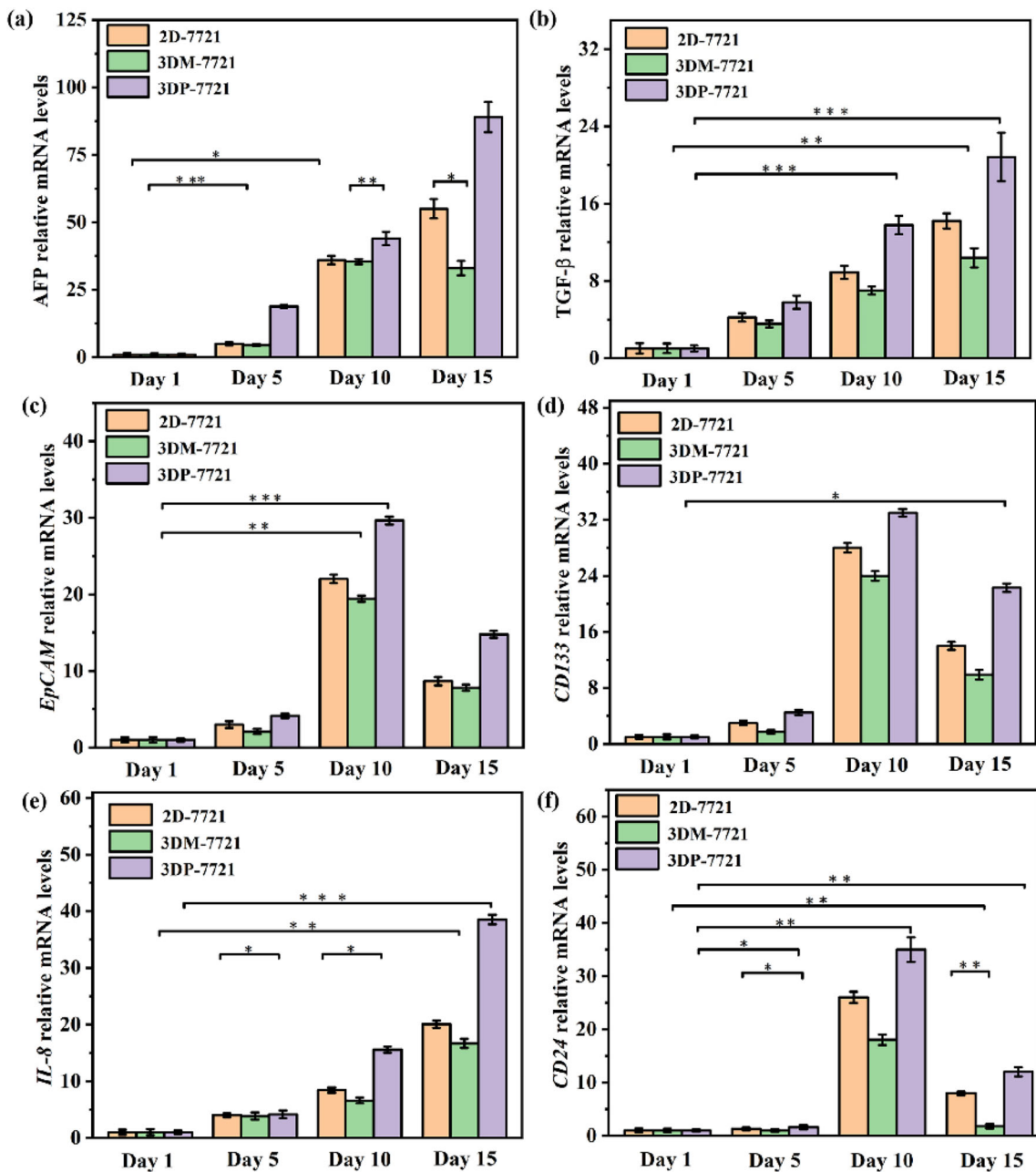
Fig. 7 mRNA expression in the liver cancer cell model created using 3D bioprinting. mRNA expression of tumor-related proteins and genes in the 2D-7721, 3DM-7721, and 3DP-7721 models on Days 1, 5, 10, and 15, including **a** AFP, **b** TGF-β, **c** *EpCAM*, **d** *CD133*, **e** *IL-8*, and **f** *CD24*. Data are presented as mean±standard deviation, $n=3$. $^{*}p<0.05$, $^{**}p<0.01$, $^{***}p<0.001$. 3D: three-dimensional; 2D-7721: two-dimensional culture model; 3DM-7721: 3D mixed culture model; 3DP-7721: 3D bioprinting model; AFP: alpha-fetal protein; TGF-β: transforming growth factor beta; *EpCAM*: epithelial cell adhesion molecule; *CD133*: prominin-1; *IL-8*: interleukin-8; *CD24*: cluster of differentiation 24
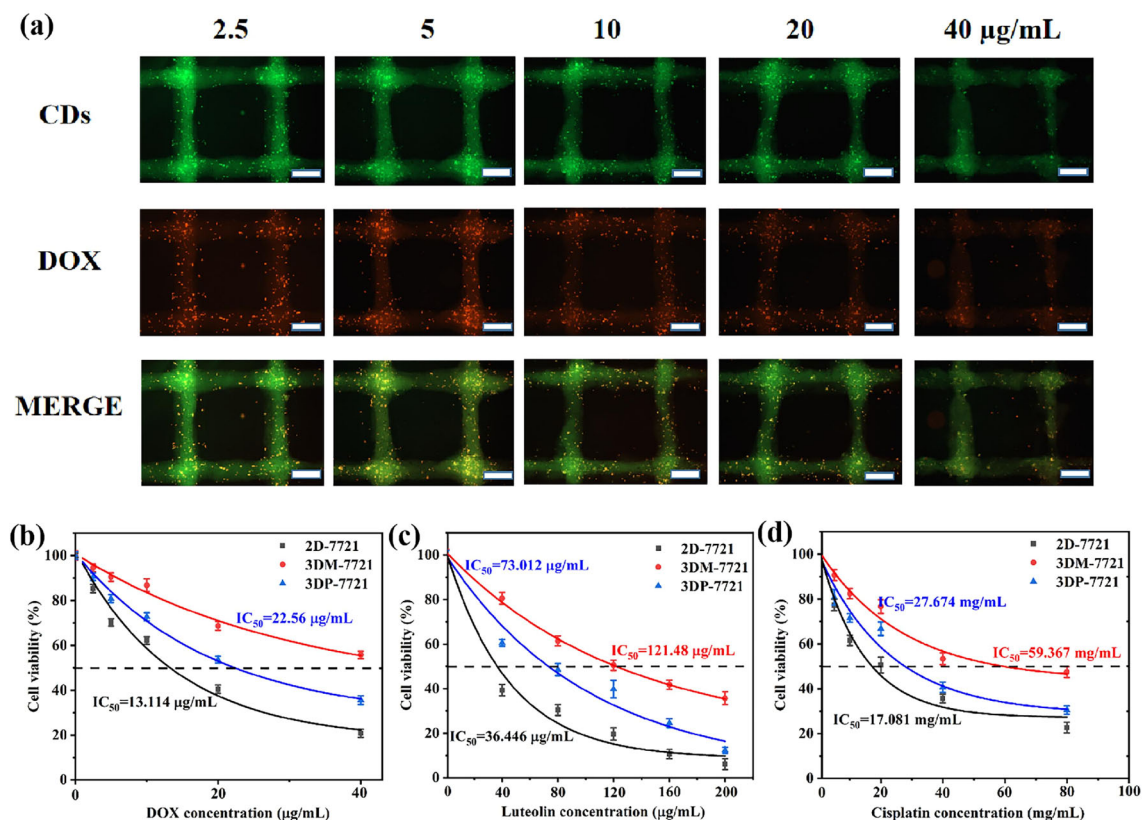
Fig. 8 a Fluorescence imaging of SMMC-7721 cells in the 3DP-7721 model incubated with different concentrations of DOX for 24 h. Scale bar: 300 μm. Dose-effect curves of **b** DOX, **c** luteolin, and **d** cisplatin in the 2D-7721, 3DM-7721, and 3DP-7721 models after 48 h of treatment. Data are presented as mean±standard deviation, *n*=4.

SMMC-7721: human hepatocarcinoma cells; CDs: carbon quantum dots; DOX: doxorubicin hydrochloride; 2D-7721: two-dimensional culture model; 3DM-7721: three-dimensional mixed culture model; 3DP-7721: 3D bioprinting model; IC_{50}: half maximal inhibitory concentration

We used HE, Ki67, *EpCAM*, *CD133*, and TUNEL immunohistochemical staining to assess the levels of the biochemical markers that are associated with the formation of solid tumors to determine the causes of the variations in the size of the solid tumors formed in the three groups. In contrast to the 3DP-7721 group, the 2D-7721 group had more loose tumors and greater necrotic regions as seen in the HE data in Fig. 10f. The extracellular matrix (ECM) components also showed directional expansion in the tumor formed from the 3DP-7721 model group, which may be related to the increased ECM remodeling capacity in 3D-printed environments. HE staining showed that the cells in the tumor tissue were densely packed and spindle shaped with large and dark nuclei. These findings suggest that the tumor cells had biological characteristics of malignant tumors in vivo. These results showed that Ki67, and the tumor stem cell markers *EpCAM* and *CD133* in the tumor cells of the 3DP-7721 model group were significantly increased, indicating that the tumor of the 3DP-7721 model group was superior to that of the other two models in terms of proliferation, invasion, metastasis, drug resistance and recurrence, and that the cancer cells of the 3DP-7721 model group had the effect of enhanced cancer stemness. Thus, the tumorigenic potential in vivo was enhanced in the 3DP-7721 model group. Additionally, TUNEL staining revealed that the 2D-7721 and 3DM-7721 groups underwent more apoptosis than the 3DP-7721 group. Overall, these results indicate that the tumor cells in the 3DP-7721 model are more tumorigenic in vivo. This may be because the cells are under closer physiological condition to that of the real tumor under 3D culture conditions, supporting the accuracy of the findings presented in this study. Consequently, 3DP-7721 tumor models offer potential for modeling animal tumors and evaluating drugs.

Conclusions

Using the 3D bioprinting technique and a composite hydrogel system of bioink that offered printability and biocompatibility, a porous hepatoma model (3DP-7721) was created in vitro. This study showed that the bioink (3:1 volume ratio of GelMA (10%, mass fraction) to PEO (1.6%, mass fraction) hydrogel) provides unique pore-forming properties, sufficient mechanical properties, and biocompatibility.
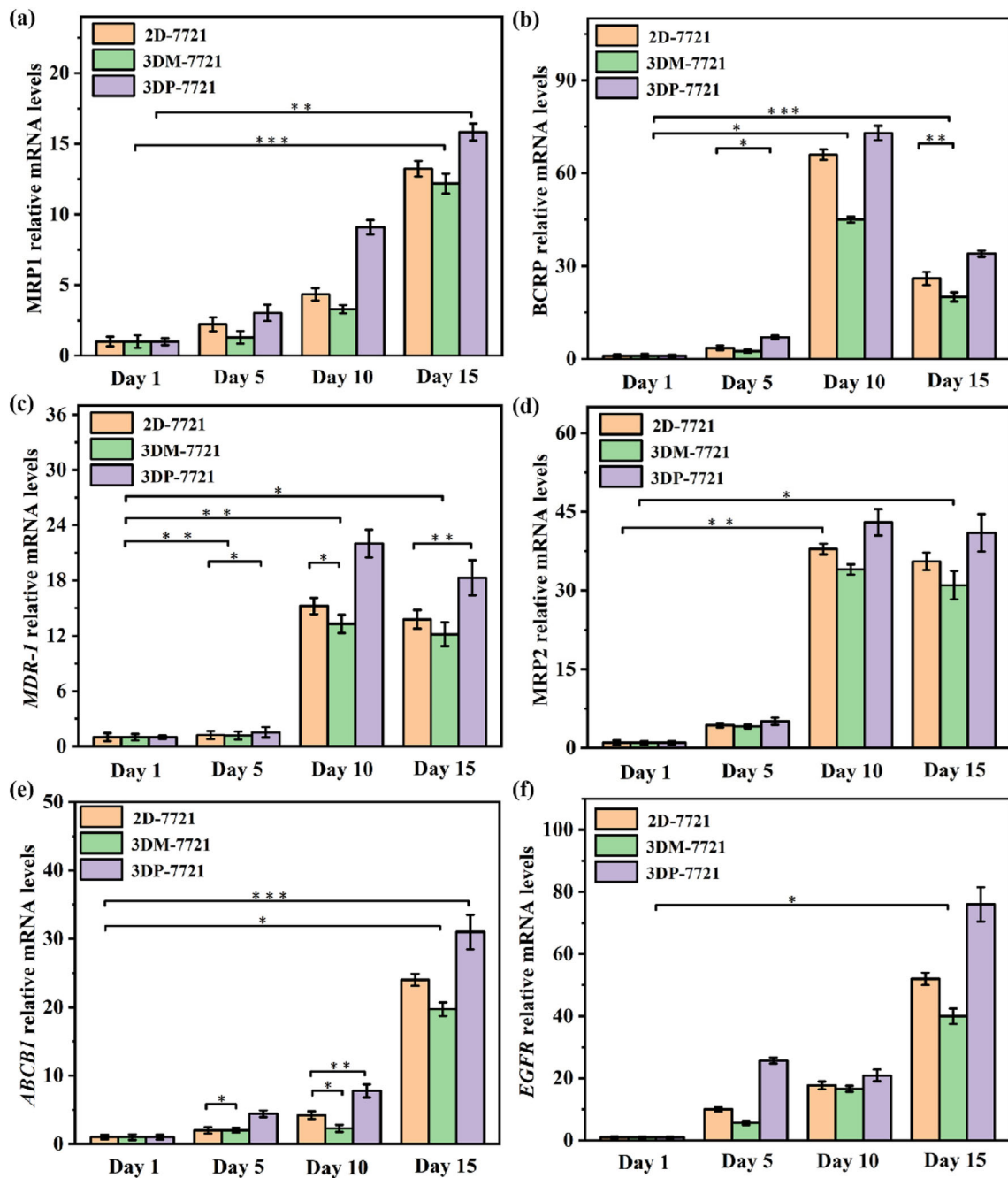
Fig. 9 mRNA expression of drug-resistant proteins and genes in the 2D-7721, 3DM-7721, and 3DP-7721 models. **a** MRP1, **b** BCRP, **c** *MDR-1*, **d** MRP2, **e** *ABCB1*, and **f** *EGFR* mRNA expression. Data are presented as mean±standard deviation, *n*=3. *p<0.05, **p<0.01, ***p<0.001. 2D-7721: two-dimensional culture model; 3DM-7721: three-dimensional mixed culture model; 3DP-7721: 3D bioprinting model; MRP1: multidrug resistance-associated protein 1; BCRP: breast cancer resistant protein; *MDR-1*: multidrug resistance 1; MRP2: multidrug resistance-associated protein 2; *ABCB1*: atp binding cassette subfamily b member 1 gene; *EGFR*: epidermal growth factor receptor
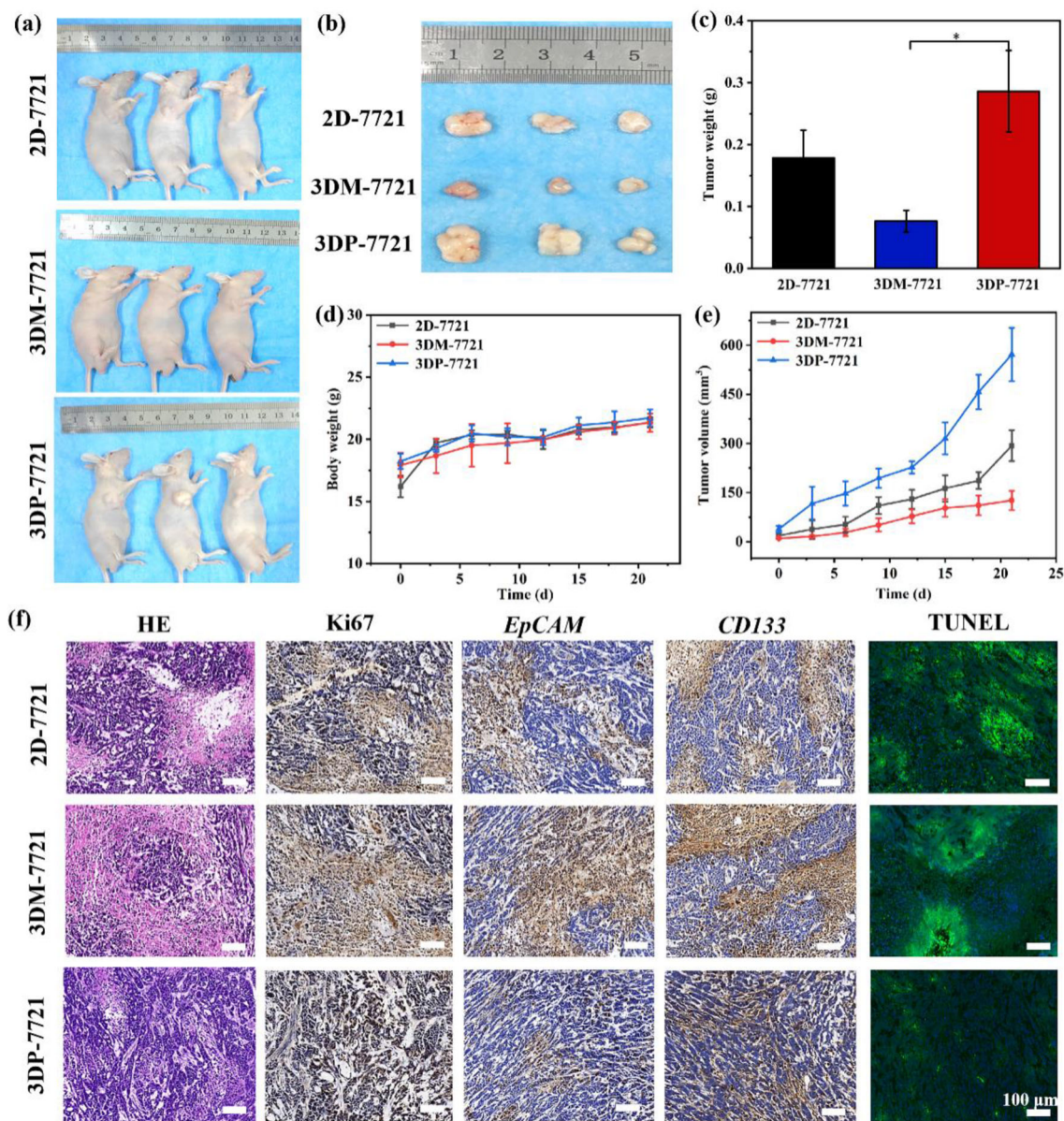
Fig. 10 Tumorigenicity of cells in different models. Photos of **a** nude mice with **b** tumors (2D-7721, 3DM-7721, and 3DP-7721 culture groups) 21 days after tumor formation. **c** Tumor weight at Day 21. Data are presented as mean±standard deviation, $n=3$. $^*p<0.05$. **d** Mouse weight and **e** tumor volume for different models at each time point. **f** HE, Ki67, *EpCAM*, *CD133*, and TUNEL staining results of solid tumors under different models. 2D-7721: two-dimensional culture model; 3DM-7721: three-dimensional mixed culture model; 3DP-7721: 3D bioprinting model; HE: hematoxylin and eosin; Ki67: proliferation marker protein Ki-67; *EpCAM*: epithelial cell adhesion molecule; *CD133*: prominin-1; TUNEL: terminal deoxynucleotidyl transferase-mediated dUTP-biotin nick end labeling assay

The 3D bioprinting process can draw silky continuous lines with excellent structural support, maintaining stability of porous structures at 20 °C with a nozzle movement speed of 13 mm/s and extrusion pressure of 1.3 bar. In this 3DP-7721 model, CDs were used for long-term cell tracking. Fluorescence imaging by CDs as well as CCK-8 detection indicated that the 3DP-7721 model supported cell proliferation. The expression of tumor-associated proteins and mRNA indicated that the 3DP-7721 model had greater levels of tumor-associated gene expression and a more tumorigenic phenotype than found in the conventional 2D-7721 and 3DM-7721 models. In addition, the cells cultured in the 3DP-7721 model had strong tumorigenicity in nude mice, showing the pathological characteristics of malignant tumors. The determination of the antitumor effects of several drug treatments confirmed that the differences in the expression levels of

tumor and cancer stem cell markers reflect the differences in the biological activities of tumor cells. The anticancer drug resistance of the SMMC-7721 cells in the 3D construct further demonstrates its biological activities; therefore, the 3DP-7721 model described in this study shows considerable potential for personalized treatment and tumorigenesis research.

This study does have some limitations. First, only one hepatocellular carcinoma (HCC) cell line was evaluated. Most importantly, multiple types of cells are present in tumors, but our 3DP-7721 model only included tumor cells. To enhance this system, our team is researching more complex tumor architectures, which include both tumor and endothelial cells and other cellular elements.

Author contributions XYW participated in conceptualization, investigation, methodology, formal analysis, investigation, and writing of the original draft. ZXL and QQD were involved in supervision, conceptualization, writing—review and editing, and funding acquisition. BYZ and YYC were involved in methodology. ZZS, ML, and YFX contributed to writing—review and editing. JMW was involved in methodology, validation, and formal analysis. SBS contributed to conceptualization, funding acquisition, supervision, and writing—review and editing.

Declarations

Conflict of interest The authors declare that they have no conflict of interest.

Ethical approval All animal procedures were performed in accordance with the Guidelines for Care and Use of Laboratory Animals of Shanxi Medical University and approved by the Animal Ethics Committee of the First Hospital of Shanxi Medical University (License number: SYXK (Jin) 2018–0001).

References

1. You L, Lv Z, Li C et al (2021) Worldwide cancer statistics of adolescents and young adults in 2019: a systematic analysis of the global burden of disease study 2019. ESMO Open 6(5):100255. https://doi.org/10.1016/j.esmoop.2021.100255
2. Ferlay J, Colombet M, Soerjomataram I et al (2021) Cancer statistics for the year 2020: an overview. Int J Cancer 149(4):778–789. https://doi.org/10.1002/ijc.33588
3. Huang H, Zhang J, Ling F et al (2021) Leptin Receptor (LEPR) promotes proliferation, migration, and invasion and inhibits apoptosis in hepatocellular carcinoma by regulating ANXA7. Cancer Cell Int 21:4. https://doi.org/10.1186/s12935-020-01641-w
4. Stock K, Estrada MF, Vidic S et al (2026) Capturing tumor complexity in vitro: comparative analysis of 2D and 3D tumor models for drug discovery. Sci Rep 6(1):28951. https://doi.org/10.1038/srep28951
5. Ma L, Li YT, Wu YT et al (2020) The construction of in vitro tumor models based on 3D bioprinting. Bio-Des Manuf 3(3):227–236. https://doi.org/10.1007/s42242-020-00068-6
6. Mao SS, He JY, Sun W et al (2022) Bioprinting of patient-derived in vitro intrahepatic cholangiocarcinoma tumor model: establishment, evaluation and anti-cancer drug testing. Biofabrication 12(4):045014. https://doi.org/10.1088/1758-5090/aba0c3
7. Brancato V, Oliveira JM, Kundu SC et al (2020) Could 3D models of cancer enhance drug screening? Biomaterials 232:119744. https://doi.org/10.1016/j.biomaterials.2019.119744
8. Ruiz-Garcia H, Alvarado-Estrada K, Trifiletti DM et al (2020) Engineering three-dimensional tumor models to study glioma cancer stem cells and tumor microenvironment. Front Cell Neurosci 14:558381. https://doi.org/10.3389/fncel.2020.558381
9. Mak IWY, Evaniew N, Ghert M (2014) Lost in translation: animal models and clinical trials in cancer treatment. Am J Transl Res 6(2):114–118
10. Mcgonigle P, Ruggeri B (2014) Animal models of human disease: challenges in enabling translation. Biochem Pharmacol 87(1):162–171. https://doi.org/10.1016/j.bcp.2013.08.006
11. Lv K, Zhu JJ, Zheng SS et al (2021) Evaluation of inhibitory effects of geniposide on a tumor model of human breast cancer based on 3D printed Cs/Gel hybrid scaffold. Mater Sci Eng C 119:111509. https://doi.org/10.1016/j.msec.2020.111509
12. Santo VE, Rebelo SP, Estrada MF et al (2017) Drug screening in 3D in vitro tumor models: overcoming current pitfalls of efficacy readouts. Biotechnol J 12(1):1600505. https://doi.org/10.1002/biot.201600505
13. Xie MJ, Gao Q, Fu JZ et al (2020) Bioprinting of novel 3D tumor array chip for drug screening. Bio-Des Manuf 3(3):175–188. https://doi.org/10.1007/s42242-020-00078-4
14. Kim J, Jang J, Cho DW (2021) Recapitulating the cancer microenvironment using bioprinting technology for precision medicine. Micromachines 12(9):1122. https://doi.org/10.3390/mi12091122
15. Msab C, Qian BA, Mmnb D et al (2021) 3D bioprinting of engineered breast cancer constructs for personalized and targeted cancer therapy. J Contr Rel 333:91–106. https://doi.org/10.1016/j.jconrel.2021.03.026
16. Shen J, Guvendiren M (2021) Complex 3D bioprinting methods. APL Bioeng 5(1):011508. https://doi.org/10.1063/5.0034901
17. Khot MI, Levenstein MA, Boer G et al (2020) Characterising a PDMS based 3D cell culturing microfluidic platform for screening chemotherapeutic drug cytotoxic activity. Sci Rep 10(1):15915. https://doi.org/10.1038/s41598-020-72952-1
18. Xie FH, Sun LJ, Pang Y et al (2020) Three-dimensional bioprinting of primary human hepatocellular carcinoma for personalized medicine. Biomaterials 265:120416. https://doi.org/10.1016/j.biomaterials.2020.120416
19. Suarez-Martinez AD, Sole-Gras M, Dykes SS et al (2020) Bioprinting on live tissue for investigating cancer cell dynamics. Tissue Eng A 27(7–8):438–453. https://doi.org/10.1089/ten.tea.2020.0190
20. Xu R, Zhou XT, Wang SK et al (2020) Tumor organoid models in precision medicine and investigating cancer-stromal interactions. Pharmacol Therapeut 218(9):107668. https://doi.org/10.1016/j.pharmthera.2020.107668
21. Nie J, Gao Q, Fu JZ et al (2020) Grafting of 3D bioprinting to in vitro drug screening: a review. Adv Healthc Mater 9(7):e1901773. https://doi.org/10.1002/adhm.201901773

22. Douglas AM, Fragkopoulos AA, Gaines MK et al (2017) Dynamic assembly of ultrasoft colloidal networks enables cell invasion within restrictive fibrillar polymers. Proc Natl Acad Sci USA 114(5):885–890. https://doi.org/10.1073/pnas.1607350114

23. Xin SJ, Wyman OM, Alge DL (2018) Assembly of PEG microgels into porous cell-instructive 3D scaffolds via thiol-ene click chemistry. Adv Healthc Mater 7(11):e1800160. https://doi.org/10.1002/adhm.201800160

24. Ying GL, Jiang N, Maharjan S et al (2018) Bioprinting: aqueous two-phase emulsion bioink-enabled 3D bioprinting of porous hydrogels. Adv Mater 30:1870382. https://doi.org/10.1002/adma.201870382

25. Sang SB, Cheng R, Cao YY et al (2022) Biocompatible chitosan/polyethylene glycol/multi-walled carbon nanotube composite scaffolds for neural tissue engineering. J Zhejiang Univ-Sci B (Biomed & Biotechnol) 23(1):58–73. https://doi.org/10.1631/jzus.B2100155

26. Ying G, Manríquez J, Wu D et al (2020) An open-source handheld extruder loaded with pore-forming bioink for in situ wound dressing. Mater Today Bio 8:100074. https://doi.org/10.1016/j.mtbio.2020.100074

27. Ying GL, Jiang N, Parra-Cantu C et al (2020) Bioprinted injectable hierarchically porous gelatin methacryloyl hydrogel constructs with shape-memory properties. Adv Funct Mater 30(46):2003740. https://doi.org/10.1002/adfm.202003740

28. Cao YY, Cheng P, Sang SB et al (2021) 3D printed PCL/GelMA biphasic scaffold boosts cartilage regeneration using co-culture of mesenchymal stem cells and chondrocytes: in vivo study. Mater Des 210:110065. https://doi.org/10.1016/j.matdes.2021.110065

29. Shen ZZ, Cao YY, Li M et al (2021) Construction of tissue-engineered skin with rete ridges using co-network hydrogels of gelatin methacrylated and poly(ethylene glycol) diacrylate. Mater Sci Eng C 129:112360. https://doi.org/10.1016/j.msec.2021.112360

30. Cheng R, Cao YY, Yan YY et al (2021) Fabrication and characterization of chitosan-based composite scaffolds for neural tissue engineering. Int J Polym Mater 71(11):831–841. https://doi.org/10.1080/00914037.2021.1915783

31. Zhang BY, Duan QQ, Zhao HC et al (2020) Application of carbon dots in nucleolus imaging to distinguish cancerous cells from normal cells. Sens Actuat B Chem 329:129156. https://doi.org/10.1016/j.snb.2020.129156

32. Zhang BY, Duan QQ, Li Y et al (2019) A "turn-on" fluorescent probe for glutathione detection based on the polyethylenimine-carbon dots-Cu^{2+} system. J Photochem Photobiol B Biol 197:111532. https://doi.org/10.1016/j.jphotobiol.2019.111532

33. Wang XY, Duan QQ, Zhang BY et al (2021) Ratiometric fluorescence detection of Cd^{2+} based on N, S co-doped carbon quantum dots/Au nanoclusters. Microchem J 167:106269. https://doi.org/10.1016/j.microc.2021.106269

34. Zhao X, Lang Q, Yildirimer L et al (2016) Photocrosslinkable gelatin hydrogel for epidermal tissue engineering. Adv Healthc Mater 5(1):108–118. https://doi.org/10.1002/adhm.201500005

35. Zhu W, Cui HT, Boualam B et al (2018) 3D bioprinting mesenchymal stem cell-laden construct with core–shell nanospheres for cartilage tissue engineering. Nanotechnology 29(18):185101. https://doi.org/10.1088/1361-6528/aaafa1

36. Livak KJ, Schmittgen TD (2001) Analysis of relative gene expression data using real-time quantitative PCR and the $2^{-\Delta\Delta C_T}$ method. Methods 25(4):402–408. https://doi.org/10.1006/meth.2001.1262

37. Ma YF, Ji Y, Zhong TY et al (2017) Bioprinting-based PDLSC-ECM screening for in vivo repair of alveolar bone defect using cell-laden, injectable and photocrosslinkable hydrogels. Acs Biomater Sci Eng 3(12):3534–3545. https://doi.org/10.1021/acsbiomaterials.7b00601

38. Ananthanarayanan B, Kim Y, Kumar S (2011) Elucidating the mechanobiology of malignant brain tumors using a brain matrix-mimetic hyaluronic acid hydrogel platform. Biomaterials 32(31):7913–7923. https://doi.org/10.1016/j.biomaterials.2011.07.005

39. Sun LJ, Yang HY, Wang YN et al (2020) Application of a 3D bioprinted hepatocellular carcinoma cell model in antitumor drug research. Front Oncol 10:878. https://doi.org/10.3389/fonc.2020.00878

40. Li Y, Farmer RW, Yang YB et al (2016) Epithelial cell adhesion molecule in human hepatocellular carcinoma cell lines: a target of chemoresistence. BMC Cancer 16(1):228. https://doi.org/10.1186/s12885-016-2252-y

41. Mima K, Baba H (2019) The gut microbiome, antitumor immunity, and liver cancer. Hepatobil Surg Nutr 8(1):67–68. https://doi.org/10.21037/hbsn.2018.11.09

42. Schomberg J, Wang Z, Farhat A et al (2020) Luteolin inhibits melanoma growth in vitro and in vivo via regulating ECM and oncogenic pathways but not ROS. Biochem Pharmacol 177(2):114025. https://doi.org/10.1016/j.bcp.2020.114025

43. Guo LW, Zheng JP, Zeng H et al (2020) Atorvastatin potentiates the chemosensitivity of human liver cancer cells to cisplatin via downregulating YAP1. Oncol Lett 21(2):82. https://doi.org/10.3892/OL.2020.12343

44. Li YJ, Lei YH, Yao N et al (2017) Autophagy and multidrug resistance in cancer. Chin J Cancer 36(1):342–351. https://doi.org/10.1186/s40880-017-0219-2

45. Lei SY, Fei R, Lei LC (2019) Autophagy elicits a novel and prospect strategy to starve arginine-dependent tumors. Hepatobil Surg Nutr 8(4):401–403. https://doi.org/10.21037/hbsn.2019.03.18

46. Fergusson JR, Ussher JE, Kurioka A et al (2018) High MDR-1 expression by MAIT cells confers resistance to cytotoxic but not immunosuppressive MDR-1 substrates. Clin Exp Immunol 194(2):180–191. https://doi.org/10.1111/cei.13165

47. Smith AG, Macleod KF (2019) Autophagy, cancer stem cells and drug resistance. J Pathol 247(5):708–718. https://doi.org/10.1002/path.5222